Editors' Suggestion

Thermalization of Two- and Three-Dimensional Classical Lattices

Zhen Wang,[1,2,*] Weicheng Fu,[3,4,*] Yong Zhang,[1,4] and Hong Zhao[1,4,†]
[1]Department of Physics, Xiamen University, Xiamen 361005, Fujian, China
[2]CAS Key Laboratory of Theoretical Physics and Institute of Theoretical Physics, Chinese Academy of Sciences, Beijing 100190, China
[3]Department of Physics, Tianshui Normal University, Tianshui 741001, Gansu, China
[4]Lanzhou Center for Theoretical Physics, Key Laboratory of Theoretical Physics of Gansu Province, Lanzhou University, Lanzhou, Gansu 730000, China

(Received 3 August 2022; revised 11 February 2024; accepted 2 May 2024; published 23 May 2024)

Understanding how systems achieve thermalization is a fundamental task in statistical physics. This Letter presents both analytical and numerical evidence showing that thermalization can be universally achieved in sufficiently large two- and three-dimensional lattices via weak nonlinear interactions. Thermalization time follows a universal scaling law unaffected by lattice structures, types of interaction potentials, or whether the lattice is ordered or not. Moreover, this study highlights the critical impact of dimensionality and degeneracy on thermalization dynamics.

DOI: 10.1103/PhysRevLett.132.217102

The energy equipartition theorem (EET), originally derived from gas models, is a cornerstone in statistical physics. The exploration of the EET in lattice models commenced in the early 1950s, following the discovery of the Fermi-Pasta-Ulam-Tsingou recurrence [1]. Extensive research in one-dimensional (1D) lattices has established that, in the thermodynamic limit, thermalization time (or energy equipartition time) typically scales as a power-law function of interaction strength, confirming the achievability of the EET [2–21]. However, condensed matter systems are often represented in higher spatial dimensions, typically in two-dimensional (2D) and three-dimensional (3D) lattice models, making the validation of the EET in these models both theoretically and practically significant. Findings from 1D models may not be directly transferable to higher dimensions due to the impact of dimensionality on physical properties, such as the dependence of thermal conductivity on dimensions [22–28]. Despite this, research on thermalization in higher-dimensional lattices remains sparse, primarily due to the complexities of numerical simulation and theoretical analysis. The most relevant contributions in this area are from Benettin and his collaborators, who investigated a hexagonal lattice with Lennard-Jones (LJ) potentials, observing energy equipartition at timescales of ϵ^{-1} for fixed or open boundaries while $\epsilon^{-5/4}$ for periodic boundaries [29,30]. Here, ϵ denotes the energy density. Additionally, studies have explored energy equipartition among flexural modes in graphene [31–33]. The effect of disorder, leading to Anderson localization and hindering energy diffusion and, thus, affecting thermalization, remains completely unexplored in high-dimensional lattices.

In this Letter, we extend these studies to typical high-dimensional lattice models, including 2D hexagonal and square lattices and 3D face-centered cubic (fcc) and simple cubic (SC) lattices. We focus on the influence of dimensionality on thermalization. Our findings reveal a universal scaling law $T_{\mathrm{eq}} \sim g^{-2}$, where T_{eq} represents thermalization time and g is the interaction strength. This law is more pronounced in higher dimensions than in 1D lattices. Importantly, we discover that degeneracy plays a crucial role: Higher degeneracy in square and SC lattices significantly accelerates the thermalization, particularly in the initial stages of energy redistribution, compared to lattices with lower degeneracy, like the hexagonal and fcc lattices. Introducing disorder may postpone the thermalization in high-degeneracy lattices while may expedite this process in low-degeneracy ones.

Our approach combines theoretical analysis with numerical simulations. Previous studies on 1D lattices have proposed several analytical methods [11,13], typically identifying the scaling from the kinetic equations for normal modes within the perturbation framework [13]. In recent studies of thermalization in 1D lattices [14–21], the wave turbulence approach [34,35] has been instrumental. It not only contributes to the derivation of kinetic equations, but also elucidates a network connecting all normal modes through multiwave resonances. This network plays a crucial role in facilitating the energy redistribution toward equilibrium. We extend this approach to high-dimensional lattices and find that, although increased spatial dimensions complicate numerical simulations, they simplify theoretical analysis. Our analysis reveals that each normal mode is intricately connected to numerous other modes. This extensive connectivity clarifies the consistence between the time scaling derived from kinetic equations and that observed for energy equipartition throughout the entire network. It also explains the accelerated thermalization observed in high-dimensional lattices. The impact

of degeneracy, we propose, stems from additional energy diffusion due to resonance among modes of the same frequency, enhancing energy redistribution further.

Without loss of generality, we adopt an n-order polynomial potential with $n \geq 3$ as the integrability-breaking term to derive the kinetic equation, since interaction potentials can be expanded as polynomial terms by the Taylor expansion. Consider a lattice described by the Hamiltonian $H = H_0 + \lambda V^{(n)}$, where

$$H_0 = \sum_{\boldsymbol{l},\alpha} \frac{1}{2} M^{\boldsymbol{l}} |\dot{\boldsymbol{u}}^{\boldsymbol{l}}|^2 + \frac{1}{4} \sum_{\substack{\boldsymbol{ll'} \\ \alpha,\beta}} [u^{\boldsymbol{l}}_{\alpha} - u^{\boldsymbol{l'}}_{\alpha}] \Phi^{\boldsymbol{ll'}}_{\alpha\beta} [u^{\boldsymbol{l}}_{\beta} - u^{\boldsymbol{l'}}_{\beta}]$$

$$\text{and} \quad V^{(n)}(u) = \frac{1}{n!} \sum_{\boldsymbol{ll'\beta}} \Phi^{\boldsymbol{ll'}}_{\boldsymbol{\beta}} \prod_{j=1}^{n} [u^{\boldsymbol{l}}_{\beta_j} - u^{\boldsymbol{l'}}_{\beta_j}], \tag{1}$$

where $\boldsymbol{l}$ is a vector indexing the particle, the Greek letters represent components of Cartesian coordinate, and $M^{\boldsymbol{l}}$ and $u^{\boldsymbol{l}}_{\alpha}$ denote, respectively, the mass and the displacement in the α direction of the $\boldsymbol{l}$th particle. The matrix elements $\Phi^{\boldsymbol{ll'}}_{\alpha\beta}$ and $\Phi^{\boldsymbol{ll'}}_{\boldsymbol{\beta}}$ are coefficients of Taylor expansion. We also use the shorthand notation $\boldsymbol{\beta} = (\beta_1, \ldots, \beta_n)$ for brevity. The parameter λ governs the interaction strength. The Hamiltonian (1) can be rescaled by the energy density ϵ. Specifically, setting $u^{\boldsymbol{l}}_{\alpha} = \tilde{u}^{\boldsymbol{l}}_{\alpha} \epsilon^{1/2}$ leads to $\tilde{H} = H/\epsilon = H_0(\dot{\tilde{u}}_{\alpha}, \tilde{u}_{\alpha}) + g V^{(n)}(\dot{\tilde{u}}_{\alpha}, \tilde{u}_{\alpha})$, where $g = \lambda \epsilon^{(n-2)/2}$ represents the interaction strength.

Considering the integrals of motion of Hamiltonian H_0 as $\{I_k\}$, we have the commutation relation $[H_0, I_k] = 0$ in terms of the Poisson bracket. In the presence of perturbation $V^{(n)}$, the system evolves following the Liouville equation [36]:

$$\partial_t I_k = L_0 I_k + L' I_k, \tag{2}$$

where L_0 and L' are Liouville operators such that $L_0 I_k = [H_0, I_k]$ and $L' I_k = \lambda [V^{(n)}, I_k]$.

The kinetic equation up to the second-order perturbation for I_k is

$$\partial_t \langle I_k \rangle \approx \langle L' I_k \rangle_{f(0)} + \int_0^{\infty} \langle L' L'(\tau) I_k \rangle_{f(t)} \mathrm{d}\tau, \tag{3}$$

where $L'(\tau) = e^{-L_0 \tau} L' e^{L_0 \tau}$ and $f(t)$ is the distribution function of the system (1). The $\langle I_k \rangle$ is the ensemble average over $f(t)$. With sufficiently weak perturbation, the dynamics are primarily governed by H_0, allowing the deformed $I_k(t)$ to be considered as the integral of motion of H_0. Consequently, the distribution can be approximated by a generalized Gibbs ensemble, expressed as

$$f(t) \sim e^{-\sum_k \theta_k(t) I_k}, \tag{4}$$

where θ_k is the Lagrange multipliers associated with I_k [37]. The role of perturbations is to drive the evolution of I_k within the space of integrals of motion of H_0.

In a lattice model, we introduce the canonical complex normal variables via $a_s(k) = P_s(k) + \mathrm{i}\omega_s(k) Q_s(k)$, where $Q_s(k)$ and $P_s(k)$ are the Fourier transforms of displacements and momenta, respectively. The term $\omega_s(k)$ denotes the dispersion relation with k and s representing the wave vector and polarization of the wave, respectively. It is important to note that k and s possess clear physical significance only in systems invariant under spatial translation; otherwise, they serve simply to order the waves. In terms of $a_s(k)$, the integrable part of the Hamiltonian is reformulated as

$$H_0 = \sum_{s,k} E_s(k) = \sum_{s,k} \omega_s(k) a_s(k) a_s^*(k). \tag{5}$$

The integral of motion of H_0 turns to be $I_s(k) = a_s(k) a_s^*(k)$. The nth-order nonlinear perturbation can be reexpressed as

$$V^{(n)} = \frac{g}{n!} \sum_{\ell=0}^{n} \sum_{1\ldots n} \binom{n}{\ell} W^{\ell+1\ldots n}_{1\ldots\ell} a_1 \ldots a_{\ell} a^*_{\ell+1} \ldots a^*_n, \tag{6}$$

where $a_j = a_{s_j}(k_j)$ is a shorthand notation and $W^{\ell+1\ldots n}_{1\ldots\ell}$ weights the transfer of energy among waves $a_1, \ldots, a_n$.

Inserting Eqs. (4)–(6) into Eq. (3), we acquire the kinetic equation for a specific integral of motion $I_1 = I_{s_1}(k_1)$ as

$$\partial_t \langle I_1 \rangle = \eta_1 - \gamma_1 \langle I_1 \rangle, \tag{7}$$

where η_1 and γ_1 are coefficients independent of $\langle I_1 \rangle$ and are proportional to g^2. Given that γ_1 is nonzero, it follows that $\langle I_1 \rangle$ relaxes at timescale approximately as $1/\gamma_1$; see Sec. I in Supplemental Material [38] for a detailed derivation of the kinetic equation.

Nonvanishing γ_1 is guaranteed by the n-wave resonance conditions:

$$\omega_1 + \cdots + \omega_{\ell} = \omega_{\ell+1} + \cdots + \omega_n, \tag{8}$$

$$k_1 + \cdots + k_{\ell} = k_{\ell+1} + \cdots + k_n. \tag{9}$$

Given that the values of $\omega_s(k)$ in large systems are densely packed and considering that nonlinearity broadens the frequency [35], the resonance condition Eq. (8) can be replaced by a quasiresonant condition:

$$|\omega_1 + \cdots + \omega_{\ell} - \omega_{\ell+1} - \cdots - \omega_n| \lesssim \Gamma, \tag{10}$$

where Γ is the resonance width.

In high-dimensional settings, the multiplicity of branches in dispersion relations facilitates identifying solutions to resonance conditions. For example, consider

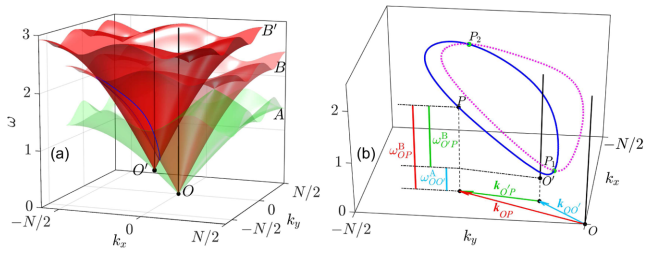

FIG. 1. Demonstration of the three-wave resonances in a hexagonal lattice. (a) displays the dispersion relation with two frequency surfaces labeled as A and B. Surface B' results from shifting the origin O to O' on surface A. (b) illustrates the intersection curves between B and B' (solid line) and between B and B'' (dashed line). Surface B'' (not depicted) is derived by further shifting the origin from O' to O'' on surface A. The two closed curves represent two groups of resonant three-wave sets, connected at points P_1 and P_2.

a hexagonal lattice with a cubic polynomial potential ($n = 3$). The dispersion relation of this lattice, obtained in the thermodynamic limit, showcases two distinct frequency surfaces labeled as A and B, as depicted in Fig. 1(a). In this limit, the frequencies densely populate these surfaces. We investigate three-wave resonant solutions using a well-established algorithm [34]. We start by moving the coordinate origin from O to O' along surface A. This shift produces new frequency surfaces, namely, A' and B'. Below, we just discuss surface B' as an example. The extension to including surface A' is straightforward; see Sec. II in Supplemental Material [38]. Note that B' intersects with the original surface B. This leads to a distinct closed curve of intersection between B' and B. This phenomenon is graphically represented in Fig. 1(a). The specific nature of this closed curve is further detailed in Fig. 1(b) with a blue solid line. At any point P on this curve, the relation $\boldsymbol{k}_{OO'} + \boldsymbol{k}_{O'P} = \boldsymbol{k}_{OP}$ and $\omega_{OO'} + \omega_{O'P} = \omega_{OP}$ is valid, as shown in Fig. 1(b). Here, the vector $\boldsymbol{k}_{OO'}$ is situated on surface A, while $\boldsymbol{k}_{OP}$ and $\boldsymbol{k}_{O'P}$ are located on surface B. This configuration indicates that each normal mode $\boldsymbol{k}_{OO'}$ on surface A resonates with a multitude of mode pairs $\boldsymbol{k}_{O'P}$ and $\boldsymbol{k}_{OP}$, forming a node of vast three-wave resonant sets.

All normal modes collectively form a fully connected network. A minor adjustment of the origin to a new point O'', close to O', leads to the formation of another closed intersection curve, depicted as a magenta dotted line in Fig. 1(b). This new curve, incorporating the mode $\boldsymbol{k}_{OO''}$, generates another vast three-wave resonant set. The geometric properties of the dispersion relation cause this curve to intersect the previous one at two specific points, P_1 and P_2. These intersections suggest a linkage between the normal modes described by these two curves. Consequently, this approach demonstrates how all normal modes on surface A are interconnected with those on surface B.

This intricate network structure, each mode acting as a node of a vast three-wave resonant set, enables energy dispersion across all modes through several cascades of three-wave resonances. The timescale $T_{\mathrm{eq}} \sim 1/\gamma_1$, as determined by Eq. (7), thus, characterizes the energy equipartition within the lattice. This analytical approach can be extended to other 2D and 3D lattices, as well as to polynomial potentials of order $n \geq 3$, given that they possess multiple dispersion relation branches. In the context of disordered systems, the resonance condition is simplified to those outlined in Eq. (8) or (10), due to the relaxed constraints on wave vectors, which enables a greater variety of modes to meet the resonance criteria. Thus, for both homogeneous and disordered lattices, T_{eq} can be rewritten as

$$T_{\mathrm{eq}} \propto g^{-2} = \lambda^{-2}\epsilon^{2-n}. \tag{11}$$

For finite-size lattices without nonlinearity, the frequencies of normal modes are discrete, limiting the general satisfaction of resonance conditions. When nonlinearity is introduced, each frequency ω_s spans a continuous spectrum within a certain range. As the lattice size N grows, the frequency space becomes increasingly dense. This density ensures that quasiresonance conditions are invariably met in sufficiently large lattices at a fixed level of nonlinearity, thereby validating the universal law described in Eq. (11). This observation also suggests that, in smaller lattices, the thermalization time scaling may diverge from the universal scaling law, particularly with sufficient weak nonlinearity.

Numerical verification.—We conducted numerical validations using two types of interaction potentials. (i) LJ potential $V(r) = [1/(1+r)^6 - 1]^2/72$, whose leading terms contribute the harmonic potential of Eq. (1) and its lowest-order anharmonic terms are cubic (terms of $V^{(3)}$): In this model, $T_{\mathrm{eq}} \sim \epsilon^{-1}$ is expected, as the higher-order terms become negligible at low energy densities. (ii) Hamiltonian (1) with a fourth-order nonlinearity $V^{(4)}(\boldsymbol{u}) = \lambda \sum_{ll'} |\boldsymbol{u}^{\boldsymbol{l}} - \boldsymbol{u}^{\boldsymbol{l}'}|^4/4$: This model excludes the three-wave resonances and is used to verify the prediction of $T_{\mathrm{eq}} \sim \epsilon^{-2}$ for thermalization dominated by four-wave resonances.

In our simulation, fixed boundary conditions are adopted. Initially, only the first 10% of modes were excited. We evolve the system using the eighth-order Yoshida method and apply a conventional method [5] to determine the equipartition time. We define spectral entropy $\zeta(t) = -\sum_k w_k(t) \log[w_k(t)]$, where $w_k(t) = \bar{E}_k(t)/[\sum_k \bar{E}_k(t)]$. Here, $E_k(t) = [P^2(k) + \omega^2(k)Q^2(k)]/2$ is the energy of the kth mode, and $\bar{E}_k(t)$ is its average in the time window of length t [39]. The degree of equipartition is characterized by $\xi(t) = N^{-1}e^{\zeta(t)}$ with $\xi(t) = 1$ characterizing the equipartition. Setting a large threshold of $\xi(t)$ may significantly extend simulation time. For hexagonal and fcc lattices, we

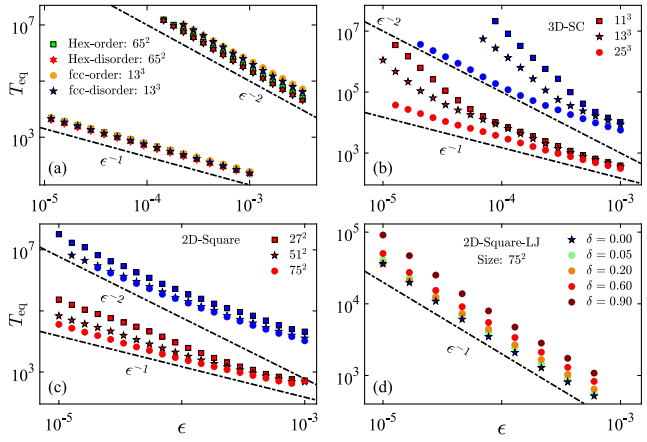

FIG. 2. Thermalization time as a function of energy density. (a) Displays results for hexagonal and fcc lattices with both homogeneous and inhomogeneous masses, where lattice sizes extend beyond the substantial influence of finite-size effects. (b) and (c) Present the findings for the square and SC lattices with homogeneous mass, respectively. (d) Shows the dependence of the thermalization time on the disorder degree for the square lattice.

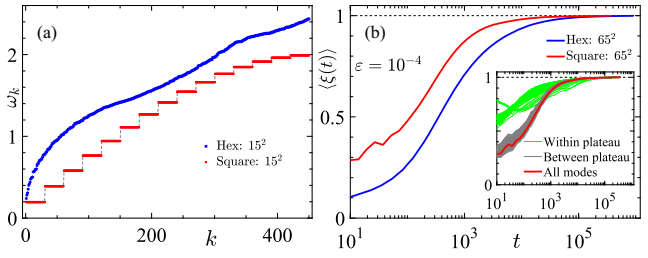

FIG. 3. (a) Ascending ordered frequencies of modes for the hexagonal and square lattices. (b) Evolution of ξ over time t for the hexagonal and square lattices. Inset: comparison of ξ evolution over time for modes within a plateau (represented in green) and for modes selected from different plateaus (in gray) for the square lattice.

confirm that further raising $\xi(t)$ from $\xi(t) = 0.5$ does not alter the scaling law of T_{eq}; thus, we apply $\xi(t) = 0.65$ as the criterion of equipartition, while for the square and SC lattices we have to set $\xi(t) = 0.95$ to determine equipartition, as lower thresholds could impact the scaling law (see Sec. III in Supplemental Material [38] for more details).

Figure 2(a) presents results for both ordered and disordered hexagonal and fcc lattices, where appropriate lattice sizes were chosen to minimize finite-size effects. In this context, *disorder* refers to masses uniformly distributed in the range $m \in (1-\delta, 1+\delta)$, where δ is a constant value less than 1. The findings align closely with theoretical expectations and show, in addition, that disorder induces an about 10% increase in thermalization speed on average. Comprehensive fitting across the energy density interval yields $T_{eq} \sim \epsilon^{-1\pm0.04}$ and $T_{eq} \sim \epsilon^{-2\pm0.05}$ for the LJ and $V^{(4)}$ potentials, respectively (see Sec. IV in Supplemental Material [38] for more details). It can be found that the thermalization time here is significantly shorter than in the counterparts of 1D case [19,21], consistent with earlier findings in hexagonal lattices [29,30]. However, thermalization time differences between 2D and 3D lattices are minor.

Figure 2(b) illustrates how thermalization time varies with system size in a uniform SC lattice. At larger sizes and lower energy densities, numerical outcomes concur with theoretical predictions, though the size necessary for convergence substantially exceeds that of the fcc lattice. At the largest system sizes achieved, we observed $T_{eq} \sim \epsilon^{-1\pm0.10}$ for the LJ potential across the entire energy range and $T_{eq} \sim \epsilon^{-2\pm0.12}$ for the $V^{(4)}$ potential at $\epsilon < 10^{-4}$.

Figure 2(c) showcases results for a uniform square lattice. For the LJ potential, alignment with theoretical predictions is evident in the largest lattice sizes, yielding $T_{eq} \sim \epsilon^{-1\pm0.10}$ at $\epsilon < 10^{-4}$. Contrastingly, for the $V^{(4)}$ potential, a noticeable slow convergence occurs, deviating from theoretical expectations even at our computational limits, with $T_{eq} \sim \epsilon^{-1.7}$ around $\epsilon \sim 10^{-5}$. At higher energy, densities approach $\epsilon \sim 10^{-3}$, and numerical results for both potentials only roughly match the predictions. Notably, in both the square and SC lattices, deviations in smaller systems are marked, as depicted in Figs. 2(b) and 2(c). Introducing disorder into the square and SC lattices results extends the thermalization time, as Fig. 2(d) shows for the square lattice as an example.

We primarily attribute these discrepancies to degeneracy. Figure 3(a) displays the frequency spectra for hexagonal and square lattices, organizing the spectral index k in ascending order to guarantee $\omega_k \leq \omega_{k+1}$. This arrangement highlights a significantly higher degeneracy in the second model. Such degeneracy manifests through the formation of distinct plateaus, where modes with matching frequencies converge. Modes within each plateau, sharing identical frequencies, facilitate rapid Chirikov resonances among them, thus promoting swift energy transfer. This observation is further supported by comparing the evolution of ξ in square and hexagonal lattices, as illustrated in Fig. 3(b), employing a LJ potential with an energy density of $\epsilon = 10^{-4}$. Analogous observations apply to fcc and SC lattices, respectively.

The inset in Fig. 3(b) explicitly contrasts the energy diffusion among modes within a plateau and across plateaus in the square lattice. It plots ξ over time, with green lines indicating ξ for modes within a plateau and gray lines for ξ of modes selected from different plateaus. The graph highlights that degenerate modes relax more rapidly. Nevertheless, the disparity in ξ within and across plateaus, or between hexagonal and square lattices, diminishes over time. Hence, while degenerated modes facilitate quick energy diffusion, the slower energy transfer across plateaus,

governed by multiwave resonance, still dictates the scaling exponent of T_{eq}. This explains the necessity for a larger threshold of ξ in lattices with high degeneracy. Introducing disorder can eliminate degeneracy to some extent and, thus, results in the increase of the thermalization time [see Fig. 2(d)].

A technique consequence of degeneracy is the requirement for significantly larger lattice sizes to reduce finite-size effects in the case of high-degeneracy lattices, as all modes within a plateau are equivalent to a single mode in a nondegenerate scenario. This fact, as well as the requirement of a larger ξ, leads to the need for larger-scale computer simulations for this type of lattices.

In summary, our theoretical analysis, building on the multiple branch structure of dispersion relations, shows that, in sufficiently large lattices under weak nonlinear interactions, all normal modes form a fully interconnected network. In this network, each mode acts as a node within broad multiwave resonant sets, leading to a general adherence to a universal thermalization time scaling law, $T_{eq} \sim g^{-2}$. This scaling law confirms the applicability of the EET in the thermodynamic limit of lattices. Unlike in 1D lattices, where segregating the Hamiltonian into integrable and nonintegrable parts is essential to observe this universal law, our numerical simulations indicate that higher-dimensional lattices naturally follow this law when employing the harmonic approximation as the integrable part. The extensive interconnectivity of each mode through multiwave resonances elucidates the accelerated thermalization observed in higher-dimensional lattices compared to their 1D counterparts.

A key discovery is the impact of degeneracy on thermalization in high dimensions, notably in lattices like square and SC, where Chirikov resonances among degenerate modes speed up thermalization. This phenomenon, acting alongside multiwave resonances, introduces an alternative mechanism for energy redistribution. Generally, the thermalization scaling remains unaffected, because the multiwave resonances, which dominate this scaling, serve as the primary mechanism for the slow energy transfer process among degenerate sets. In certain cases, especially with relatively large interaction strength, however, it may lead to a modification in the scaling law, with $T_{eq} \sim g^{-b}$, where $b < 2$. Introducing relatively small disorder may enhance the thermalization for low-degeneracy lattices, as it causes the relaxation of resonance conditions. On the contrary, introducing disorder may postpone the thermalization for high-degeneracy lattices since its degeneration-relieving effect.

Future research should address several areas: the role of higher-order multiwave resonances in energy transfer, the details of effect of degeneracy on thermalization rate and the time scaling in high-degeneracy lattices, and the implications for real-world materials. Additionally, exploring higher energy densities, including the impact of many-body localization and breathers, remains crucial. Finally, understanding the impact of boundary conditions on thermalization, identifying different mechanisms for energy diffusion, and effectively eliminating finite-size effects in highly degenerate lattices will require much larger-scale numerical simulations.

This work was supported by the National Science Foundation of China (Grants No. 12247106, No. 11975190, No. 12005156, No. 11925507, No. 12047503, and No. 12247101); the Natural Science Foundation of Gansu Province (Grant No. 21JR1RE289); the Innovation Fund from Department of Education of Gansu Province (Grant No. 2023A-106); the Project of Fu-Xi Scientific Research Innovation Team, Tianshui Normal University (Grant No. FXD2020-02); and the Education Project of Open Competition for the Best Candidates from Department of Education of Gansu Province (Grant No. 2021jyjbgs-06). W. F. also acknowledge support by the Youth Talent (Team) Project of Gansu Province, China.

*These authors contributed equally to this work.
†zhaoh@xmu.edu.cn

[1] E. Fermi, J. Pasta, and S. Ulam, Los Alamos Scientific Laboratory, Report No. LA-1940, 1955, https://dx.doi.org/10.2172/4376203.
[2] F. Izrailev and B. V. Chirikov, Dokl. Akad. Nauk **166**, 57 (1966), https://ui.adsabs.harvard.edu/abs/1966SPhD...11...30I.
[3] G. Benettin, Physica (Amsterdam) **13D**, 211 (1984).
[4] G. Benettin, R. Livi, and A. Ponno, J. Stat. Phys. **135**, 873 (2008).
[5] G. Benettin and A. Ponno, J. Stat. Phys. **144**, 793 (2011).
[6] G. Benettin, H. Christodoulidi, and A. Ponno, J. Stat. Phys. **152**, 195 (2013).
[7] C. Danieli, T. Mithun, Y. Kati, D. K. Campbell, and S. Flach, Phys. Rev. E **100**, 032217 (2019).
[8] C. Danieli, D. K. Campbell, and S. Flach, Phys. Rev. E **95**, 060202(R) (2017).
[9] J. DeLuca, A. J. Lichtenberg, and S. Ruffo, Phys. Rev. E **51**, 2877 (1995).
[10] J. DeLuca, A. J. Lichtenberg, and S. Ruffo, Phys. Rev. E **60**, 3781 (1999).
[11] G. Y. Tsaur and J. Wang, Phys. Rev. E **54**, 4657 (1996).
[12] G. Parisi, Europhys. Lett. **40**, 357 (1997).
[13] S. Lepri, Phys. Rev. E **58**, 7165 (1998).
[14] M. Onorato, L. Vozella, D. Proment, and Y. V. Lvov, Proc. Natl. Acad. Sci. U.S.A. **112**, 4208 (2015).
[15] L. Pistone, M. Onorato, and S. Chibbaro, Europhys. Lett. **121**, 44003 (2018).
[16] Y. V. Lvov and M. Onorato, Phys. Rev. Lett. **120**, 144301 (2018).
[17] W. Fu, Y. Zhang, and H. Zhao, New J. Phys. **21**, 043009 (2019).
[18] W. Fu, Y. Zhang, and H. Zhao, Phys. Rev. E **100**, 052102 (2019).

[19] W. Fu, Y. Zhang, and H. Zhao, Phys. Rev. E **100**, 010101(R) (2019).
[20] L. Pistone, S. Chibbaro, M. D. Bustamante, Y. V. Lvov, and M. Onorato, Math. Biosci. Eng. **1**, 672 (2019).
[21] Z. Wang, W. Fu, Y. Zhang, and H. Zhao, Phys. Rev. Lett. **124**, 186401 (2020).
[22] S. Lepri, R. Livi, and A. Politi, Phys. Rev. Lett. **78**, 1896 (1997).
[23] B. Hu, B. Li, and H. Zhao, Phys. Rev. E **57**, 2992 (1998).
[24] H. Zhao, Phys. Rev. Lett. **96**, 140602 (2006).
[25] S. Lepri, R. Livi, and A. Politi, Phys. Rep. **377**, 1 (2003).
[26] A. Dhar, Adv. Phys. **57**, 457 (2008).
[27] S. Lepri, ed., *Thermal Transport in Low Dimensions: From Statistical Physics to Nanoscale Heat Transfer*, Lecture Notes in Physics Vol. 921 (Springer, New York, 2016), 10.1007/978-3-319-29261-8.
[28] S. Lepri, R. Livi, and A. Politi, Phys. Rev. Lett. **125**, 040604 (2020).
[29] G. Benettin and G. Gradenigo, Chaos **18**, 013112 (2008).
[30] G. Benettin, Chaos **15**, 015108 (2005).
[31] D. Midtvedt, A. Croy, A. Isacsson, Z. Qi, and H. S. Park, Phys. Rev. Lett. **112**, 145503 (2014).
[32] Y. Wang, Z. Zhu, Y. Zhang, and L. Huang, Phys. Rev. E **97**, 012143 (2018).
[33] Y. Wang, Z. Zhu, Y. Zhang, and L. Huang, Appl. Phys. Lett. **112**, 111910 (2018).
[34] V. E. Zakharov, V. S. L'Vov, and G. Falkovich, *Kolmogorov Spectra of Turbulence I. Wave Turbulence* (Springer, Berlin, 1992), 10.1007/978-3-642-50052-7.
[35] S. Nazarenko, ed., *Wave Turbulence*, Lecture Notes in Physics Vol. 825 (Springer Verlag, Berlin, 2011), 10.1007/978-3-642-15942-8.
[36] R. Zwanzig, *Nonequilibrium Statistical Mechanics* (Oxford University Press, New York, 2001), Chap. 6, pp. 121–122, 10.1093/oso/9780195140187.001.0001.
[37] T. V. Dudnikova, A. I. Komech, and H. Spohn, J. Math. Phys. (N.Y.) **44**, 2596 (2003).
[38] See Supplemental Material at http://link.aps.org/supplemental/10.1103/PhysRevLett.132.217102 for the derivation of kinetic equation (7), analysis of three-wave resonances in a 2D hexagonal lattice, scaling of thermalization times under various thresholds, comparisons of finite size effects, verification of finite size effects and comparisons of order and disorder.
[39] R. Livi, M. Pettini, S. Ruffo, M. Sparpaglione, and A. Vulpiani, Phys. Rev. A **31**, 1039 (1985).